Efficient Numerical Modeling of Photonic Crystal Heterostructure Devices

Zhen Hu and Ya Yan Lu

***Abstract*—Photonic crystal (PhC) heterostructures combining segments of slightly different PhCs have been used to develop photonic devices, such as high-performance add/drop filters and microcavities with ultra-high quality factors. In this paper, we present a highly efficient computational method for simulating PhC heterostructure devices based on a two-dimensional (2D) model. The method delivers high-accuracy results with ultra-small computational domains and an exponential convergence rate, and it takes full advantage of the existence of many identical unit cells and the circular shape of the air-holes in typical slab-based PhC heterostructure devices. The 2D model can capture many features of realistic PhC heterostructure devices fabricated on silicon slabs. Our method can be used to explore a large number of parameters in the design and optimization process.**

***Index Terms*—Photonic crystals, hetreostructures, microcavities, waveguides, numerical methods.**

I. Introduction

In recent years, photonic crystal (PhC) heterostructures [1]–[3] have been used to develop high-performance photonic devices for some potentially important applications. A PhC heterostructure device is usually fabricated on a dielectric slab, and it consists of a number segments where each segment is a PhC possibly with some defects. An important advantage of PhC heterostructures is that out-of-slab radiation losses can be very small if the PhCs in different segments differ only slightly. This has led to the realization of mode-gap cavities with extremely large quality factors [4]–[6] and highly efficient add-drop filters [7]–[9]. PhC cavities with high quality factors and small mode volumes can significantly enhance the interaction between light and the host media, leading to many applications in nonlinear optics, quantum optics, lasing, sensing, etc. [10]–[12].

To design and optimize PhC heterostructure devices, efficient numerical methods are essential. Realistic PhC heterostructure devices based on high-index dielectric slabs are three-dimensional structures that require full-vector three-dimensional (3D) simulations. Unfortunately, 3D simulations are very expensive for practical PhC devices, due to the complexity of the structures (high index-contrast, curved interfaces, sharp edges) and the periodic PhC waveguides serving as input and output ports. In particular, if the computational domain is too small, reflections from the boundaries that terminate the PhC waveguides can produce large errors. The perfectly matched layer (PML) [13], [14] technique is widely used to truncate unbounded domains in numerical simulations of waves, but it is not effective for terminating periodic waveguides [15], [16].

For PhC devices based on slabs, light is mostly confined to the slab. Therefore, a two-dimensional (2D) model may be able to capture many features of the device. For PhC slabs with air-hole arrays, a simple 2D model is a Helmholtz equation derived by the effective index method or its enhancements [17]–[25]. Clearly, a 2D Helmholtz equation cannot be used to rigorously analyze out-of-slab radiation losses, but it can be used to model lightwave phenomena that are mostly confined to the slab and gain physical insight. For design and optimization of PhC devices, repeated simulations with different design parameters are necessary. A 2D model can be used to explore a large parameter space and to identify potentially useful designs which can be further improved by more accurate 3D simulations.

While 2D Helmholtz equations are much easier to solve than the 3D Maxwell's equations, efficient computational methods are still needed. Time-domain methods based on finite difference [26] and discontinuous Galerkin [27]–[29] techniques, are popular, but large computational domains are needed for proper modeling of outgoing waves in photonic crystal waveguides. In the frequency domain, the finite element method [30] is versatile and widely used, but some special methods for PhCs can be far more efficient [31], [32]. In Ref. [33], we developed the so-called Dirichlet-to-Neumann (DtN) map method for idealized 2D devices in a single background PhC. The method is particularly efficient, because it takes advantage of the many identical unit cells, uses analytic solutions in unit cells with circular cylinders, and truncates PhC waveguides by rigorous boundary conditions. The computational domain of the DtN-map method is much smaller than other methods, and only the unknown field on the edges of the unit cells are solved. This leads to relatively small linear systems even when the PhC devices are many times larger than the wavelength. Furthermore, the linear systems have sparse coefficient matrices, and can be efficiently solved.

In this paper, we extend the DtN-map method to PhC heterostructure devices. In particular, we analyze PhC waveguides, waveguide junctions, mode-gap cavities, and waveguide-cavity systems, all in PhC heterostructures. Although these calculations are based on a 2D Helmholtz equation, they are related to experimental results.

II. DtN maps and PhC waveguides

For idealized 2D structures which are invariant in the z direction and for H polarized light propagating in the xy

This work was supported by the National Natural Science Foundation of China under project 11101122, and the Research Grants Council of Hong Kong Special Administrative Region, China, under project CityU 102411.

Z. Hu is with the Department of Mathematics, Hohai University, Nanjing, Jiangsu, China (e-mail: huzhen1230@gmail.com).

Y. Y. Lu is with the Department of Mathematics, City University of Hong Kong, Kowloon, Hong Kong (e-mail: mayylu@cityu.edu.hk).

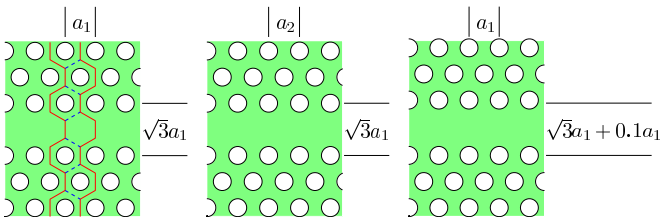

(a) PhCW1 (b) PhCW2 (c) PhCW3

Fig. 1. Three different PhC waveguides. PhCW1: standard line-defect waveguide; PhCW2: horizontally stretched waveguide; PhCW3: waveguide with increased core width. The x and y axes point to the horizontal and vertical directions, respectively.

plane, where $\{x, y, z\}$ is a Cartesian coordinate system, the governing equation in the frequency domain is the Helmholtz equation

$$\frac{\partial}{\partial x}\left(\frac{1}{n^2}\frac{\partial u}{\partial x}\right) + \frac{\partial}{\partial y}\left(\frac{1}{n^2}\frac{\partial u}{\partial y}\right) + k_0^2\, u = 0, \qquad (1)$$

where $k_0 = \omega/c$ is the free space wavenumber, ω is the angular frequency, c is the speed of light in vacuum, $n = n(x, y)$ is the refractive index function, u is the z component of the magnetic field, and the assumed time dependence is $e^{-i\omega t}$. For a PhC slab with a biperiodic array of air-holes, Eq. (1) can be regarded as a simple 2D model [17]–[25], where n in the slab region is the effective index n_e of the fundamental propagating mode of the slab (as a planar waveguide), and $n = 1$ in the holes.

PhC heterostructures may use PhCs with slightly different periodicity, and the so-called mode-gap cavities reply on waveguides in these different PhCs. In Fig. 1, we show three PhC waveguides. The first waveguide shown in Fig. 1(a) is a standard line-defect waveguide, where the background PhC is a triangular lattice of air-holes in a dielectric medium and the lattice constant is a_1. The waveguide is simply formed by filling a row of air-holes, and it is periodic in the x (horizontal) direction with period a_1. In Fig. 1(a), we also show one period of the waveguide as the region bounded by the two red curves, and that region is further divided into hexagon unit cells. There are only two different types of unit cells, i.e., the unit cells with or without a hole. All unit cells are regular hexagons with edge length $a_1/\sqrt{3}$. The PhC waveguide shown in Fig. 1(b) is obtained by increasing the x-period of the first waveguide to a_2 ($a_2 > a_1$), and keeping the original period in the y (vertical) direction. One period of this waveguide is still the union of hexagon unit cells, but these cells are not regular hexagons. They are horizontally stretched, so that the distance between the two vertical edges is a_2. The third waveguide shown in Fig. 1(c) is obtained by increasing the width of the standard line-defect waveguide by $0.1a_1$. The background PhC is identical to that of the first waveguide, i.e., it is a regular triangular lattice of air-holes with lattice constant a_1. One period of that waveguide contains one special vertically stretched unit cell (without a hole) corresponding to the waveguide core. In the following, we use the DtN-map method to calculate the guided modes in these three waveguides.

The DtN-map method was first developed for computing transmission and reflection spectra of finite 2D PhCs [34] and band structures of infinite PhCs [35]. Since then, the method has been extended to analyze PhC waveguides [36], microcavities [37], and general PhC devices [33]. In the following, we give a brief outline of the DtN-map method for analyzing PhC waveguides. More details are given in Refs. [33], [36].

The key ingredient of the method is the DtN maps of the unit cells. For a unit cell Ω, the DtN map is an operator $\mathbf{\Lambda}$ that maps the wave field to its normal derivative on the boundary of Ω. For the H polarization, we have

$$\mathbf{\Lambda}\, u = \frac{\partial u}{\partial \nu} \quad \text{on} \quad \partial\Omega, \qquad (2)$$

where u satisfies Eq. (1) in Ω, $\partial\Omega$ is the boundary of Ω, and $\partial_\nu u$ is the normal derivative of u. In practice, $\mathbf{\Lambda}$ is approximated by a small matrix. For unit cells with a circular cylinder (rods or holes), the DtN maps can be constructed from cylindrical wave expansions [34], [35]. For the PhC waveguide shown in Fig. 1(a), we follow the unit cells and consider one period of the waveguide (denoted by S) as shown in Fig. 1(a) and also in Fig. 2 where the x axis is in the vertical direction.

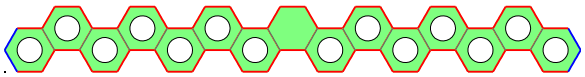

Fig. 2. One period of a PhC waveguide in a bulk PhC with a triangular lattice of air-holes. The x axis is in the vertical direction.

The transverse direction is truncated with $N_t = 7$ unit cells remaining in each side of the waveguide core. Let Γ_0 and Γ_1 be the lower and upper boundaries of domain S shown as the red curves in Fig. 2, and assuming $u = 0$ on the lateral boundaries of S (blue curves in Fig. 2), we can construct an operator $\mathbf{M}$ (also approximated by a matrix) from the DtN maps of the unit cells, such that

$$\mathbf{M}\begin{bmatrix} u|_{\Gamma_0} \\ u|_{\Gamma_1} \end{bmatrix} = \begin{bmatrix} \partial_\nu u|_{\Gamma_0} \\ \partial_\nu u|_{\Gamma_1} \end{bmatrix}. \qquad (3)$$

If u is a Bloch mode of the PhC waveguide with a Bloch wavenumber β, then

$$u|_{\Gamma_1} = \rho\, u|_{\Gamma_0}, \quad \partial_\nu u|_{\Gamma_1} = \rho\, \partial_\nu u|_{\Gamma_0}, \qquad (4)$$

where $\rho = e^{i\beta a_1}$. The above relations allow us to re-write Eq. (3) as a generalized eigenvalue problem

$$\begin{bmatrix} \mathbf{M}_{11} & -\mathbf{I} \\ \mathbf{M}_{21} & 0 \end{bmatrix}\begin{bmatrix} u|_{\Gamma_0} \\ \partial_\nu u|_{\Gamma_0} \end{bmatrix} = \rho \begin{bmatrix} -\mathbf{M}_{12} & 0 \\ -\mathbf{M}_{22} & \mathbf{I} \end{bmatrix}\begin{bmatrix} u|_{\Gamma_0} \\ \partial_\nu u|_{\Gamma_0} \end{bmatrix}, \qquad (5)$$

where $\mathbf{I}$ is the identity operator, $\mathbf{M}_{jk}$ (for j, $k = 1$, 2) are the blocks of $\mathbf{M}$.

Following the work of Song *et al.* [4], we let $a_1 = 410\,\text{nm}$, $a_2 = 420\,\text{nm}$ and $r = 0.29a_2$ (r is the radius of the air-holes) for all three waveguides shown in Fig. 1. The refractive index (outside the holes) used in the 2D Helmholtz equation (1) is assumed to be $n_e = 2.76$. Using the DtN-map method, we analyze these three PhC waveguides. The dispersion relations of the propagating Bloch modes (corresponding to a real β and

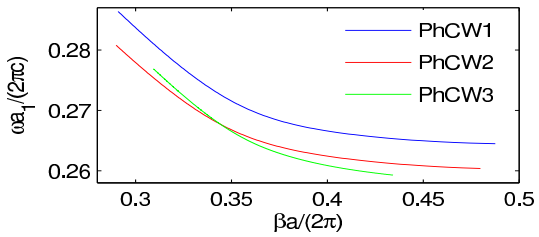

Fig. 3. Calculated dispersion curves for waveguides PhCW1, PhCW2 and PhCW3. The horizontal axis is $\beta a/(2\pi)$ where $a = a_1$ for PhCW1 and PhCW3, and $a = a_2$ for PhCW2.

$|\rho| = 1$) are shown in Fig. 3. These results are obtained using $N_p = 7$ points on each edge of the unit cells. The DtN maps of the unit cells are constructed from cylindrical wave expansions as in [34], [35], and approximated by 42×42 matrices. The operator $\mathbf{M}$ is approximated by a 406×406 matrix. Its blocks $\mathbf{M}_{jk}$ (j, $k = 1$, 2) are 203×203 matrices. Even though some unit cells for the second and third waveguides are not regular hexagons, the cylindrical wave expansions still have exponential convergence. For $N_p = 7$, the wave field in the unit cells are approximated by a linear combination of $6N_p = 42$ cylindrical waves, and resulting DtN maps are sufficiently accurate.

From Fig. 3, a frequency interval F_g can be identified where the first waveguide has no propagating mode, but the second waveguide still has a propagating mode. This interval is given by $0.2604 < \omega a_1/(2\pi c) < 0.2645$. It is related to the different mode-gaps of these two waveguides. Note that the mode-gap of a PhC waveguide is the subinterval of the relevant bandgap (of the surrounding PhC) where the waveguide does not have a propagating mode.

III. Waveguide Discontinuities

A simple PhC heterostructure can be formed if two semi-infinite PhC waveguides are put together. In Fig. 4, we show a heterostructure where the left and right half-planes correspond to the PhC waveguides shown in Fig. 1(b) and Fig. 1(a),

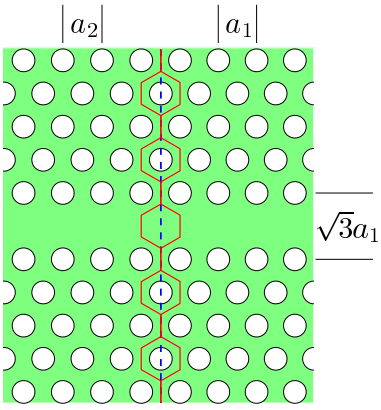

Fig. 4. Waveguide discontinuity in a PhC heterostructure. The left and right half planes are the PhC waveguides shown in Fig. 1(b) and Fig. 1(a), respectively.

respectively. Therefore, the PhC in the right half-plane has a regular triangular lattice of air-holes with lattice constant a_1, and the PhC in the left half-plane is obtained by stretching the period in the horizontal direction to a_2. The dashed line (at $x = 0$) is the interface between the two waveguides. From the results shown in Fig. 3, we expect that when the normalized frequency is in the interval $F_g = (0.2604, 0.2645)$, an incoming propagating mode in the left waveguide will be completely reflected back, but if the frequency is above the upper limit of F_g, the mode will be able to transmit to the right waveguide. Therefore, it is interesting to calculate the transmission and reflection spectra for frequencies in and above F_g.

The incident and reflected waves in the left waveguide can be written down using the Bloch modes of the waveguide:

$$u^{(i)}(x,y) = \phi_1^{(2)}(x,y)e^{i\beta_1^{(2)}x}, \quad x < 0, \tag{6}$$

$$u^{(r)}(x,y) = \sum_{j=1}^{\infty} B_j \phi_j^{(2)}(x,y)e^{-i\beta_j^{(2)}x}, \quad x < 0, \tag{7}$$

where $\beta_1^{(2)}$ is real, $\mathrm{Im}[\beta_j^{(2)}] > 0$ for all $j \neq 1$, $\phi_j^{(2)}$ is periodic in x with period a_2, and B_j are the unknown expansion coefficients. Notice that $\beta_1^{(2)}$ is chosen so that the Bloch mode $\phi_1^{(2)}e^{i\beta_1^{(2)}x}$ carries positive power in the x direction. It turns out that we should choose a negative value for $\beta_1^{(2)}$. This is also related to the negative slopes of the dispersion curves shown in Fig. 3. The transmitted wave in the right waveguide can be written as

$$u^{(t)}(x,y) = \sum_{j=1}^{\infty} C_j \phi_j^{(1)}(x,y)e^{i\beta_j^{(1)}x}, \quad x > 0, \tag{8}$$

where $\beta_1^{(1)}$ is real (actually $\beta_1^{(1)} < 0$) for frequencies above F_g, $\mathrm{Im}[\beta_j^{(1)}] > 0$ for $j \neq 1$ and for $j = 1$ if the frequency is in F_g, $\phi_j^{(1)}$ is periodic in x with period a_1, and C_j are the unknown expansion coefficients. We have used the superscripts (1) and (2) to distinguish the Bloch modes in the first and second waveguides as shown in Fig. 1. The normalized power reflection coefficient is $R = |B_1|^2$. For frequencies above F_g, the transmission coefficient T is the product of $|C_1|^2$ with the ratio of the powers carried by the propagating Bloch modes of the two waveguides.

The heterostructure shown in Fig. 4 can be divided into hexagon unit cells (with or without a hole). The unit cells in the right half-plane are regular hexagons with edge length $a_1/\sqrt{3}$. The distance between any pair of opposite edges of the unit cell is a_1. In the left half-plane, the unit cells are horizontally stretched hexagons, such that the distance between the two opposite vertical edges is a_2. Around the interface at $x = 0$, we have a set of special hexagon unit cells, as shown in Fig. 4, for which only the left half is stretched. The length of the two vertical edges is still $a_1/\sqrt{3}$, and their x-coordinates are $-a_2/2$ and $a_1/2$, respectively. These special unit cells are bounded and connected by the red edges shown in Fig. 4.

Along the red edges in Fig. 4, two continuous curves Γ_0 and Γ_1 can be identified as the boundaries of the left and right PhC waveguides. Both Γ_0 and Γ_1 contain the vertical edges at $x = 0$ (they coincide there), and they further contain

the three left and three right edges of each special unit cell, respectively. For the right semi-infinite PhC waveguide, we can establish a rigorous boundary condition

$$\frac{\partial u}{\partial \nu} = \mathbf{L}_1^+ u \quad \text{on} \quad \Gamma_1, \tag{9}$$

where $\mathbf{L}_1^+$ is an operator and it is approximated by a matrix in practice. Equation (9) relies on the Bloch mode expansion (8). To calculate $\mathbf{L}_1^+$, we start from the operator $\mathbf{M}$ for one period of the waveguide, compute the Bloch modes from eigenvalue problem (5), the use $\mathbf{M}$ and the expansion (8) to construct $\mathbf{L}_1^+$. The details are given in our earlier work [33]. On Γ_0, we have a similar boundary condition for terminating the left semi-infinite PhC waveguide:

$$\frac{\partial u}{\partial \nu} = \mathbf{L}_2^- u + g \quad \text{on} \quad \Gamma_0. \tag{10}$$

The operator $\mathbf{L}_2^-$ is related to the reflected wave as given in (7). For $\mathbf{L}_1^+$ and $\mathbf{L}_2^-$, the subscripts (1 or 2) correspond to the waveguides shown in Fig. 1 and the superscripts ($+$ or $-$) indicate the directions for which the semi-infinite waveguides extend to. Since the left waveguide contains an incident wave, the boundary condition (10) has an inhomogeneous term g. For more details, we refer the readers to Ref. [33].

For each special (half-regular and half-stretched) hexagon unit cell Ω_j, we can find a DtN map $\mathbf{\Lambda}_j$ satisfying an equation like (2). These special unit cells are bounded by Γ_0 and Γ_1. Therefore, on each edge of a special unit cell, we can evaluate $\partial_\nu u$ using the DtN map, and by Eq. (9) or Eq. (10). On a common vertical edge of Γ_0 and Γ_1 at $x = 0$, $\partial_\nu u$ can be evaluated using both Eqs. (9) and (10). Equating the two expressions of $\partial_\nu u$ on each red edges shown in Fig. 4, we obtain a linear system

$$\mathbf{A}\boldsymbol{u} = \boldsymbol{f}, \tag{11}$$

where $\boldsymbol{u}$ stands for u on all red edges in Fig. 4.

As in the previous section, we assume $a_1 = 410\,\text{nm}$, $a_2 = 420\,\text{nm}$, $r = 0.29a_2$ and $n_e = 2.76$, truncate the y direction by keeping $N_t = 7$ unit cells in each side of the waveguide core, and discretize each edge of the unit cells by $N_p = 7$ points. In that case, the curves Γ_0 and Γ_1 each contain 29 edges, the operators $\mathbf{L}_1^+$ and $\mathbf{L}_2^-$ are approximated by 203×203 matrices. There are a total of 50 red edges in Fig. 4. Therefore, $\mathbf{A}$ is a 350×350 matrix and $\boldsymbol{u}$ is a vector of length 350. From the solution $\boldsymbol{u}$, the expansion coefficients B_j and C_j can be constructed. In Fig. 5, we show the transmission and

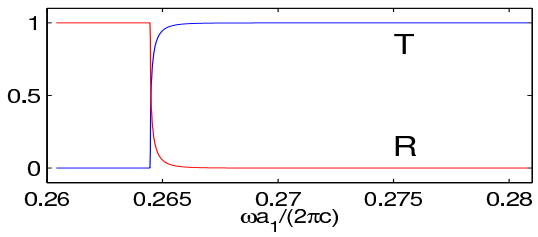

Fig. 5. Transmission and reflection spectra of a waveguide discontinuity in a PhC heterostructure.

reflection spectra of the waveguide discontinuity. Clearly, a perfect reflection occurs for frequencies in the interval F_g. When the frequency is larger than the upper limit of F_g, i.e., $\omega a_1/(2\pi c) = 0.2645$, there is a sharp drop in the reflection coefficient. The power balance law $T + R = 1$ is satisfied to high precision.

In [2], Song *et al.* reported experimental and numerical results for a slightly different waveguide discontinuity involving two PhCs with lattice constants a_1 and a_2. Both PhCs have regular triangular lattices of air-holes. Since the periods in the y direction of these two PhCs are different, there is a lattice mismatch at the interface. Nevertheless, a sharp transition from 0 to 1 is observed in the transmission spectrum.

IV. Mode-gap cavities

When the frequency is in the interval F_g, light cannot propagate in the first PhC waveguide shown in Fig. 1(a), but can still propagate in the second waveguide shown in Fig. 1(b). A mode-gap cavity is created to hold light in a small segment of the second waveguide by connecting it to two semi-infinite segments of the first waveguide. In Fig. 6, we show a mode-

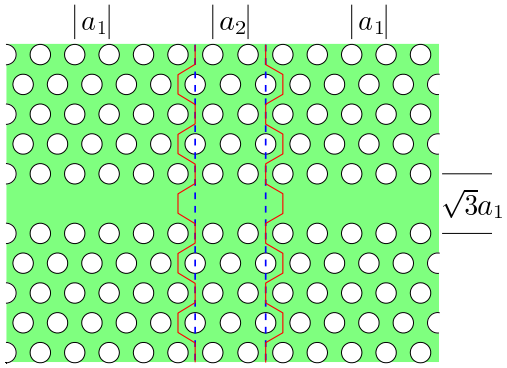

Fig. 6. A mode-gap cavity constructed by connecting a small segment (length $2a_2$) of PhCW2 with two semi-infinite segments of PhCW1.

gap cavity where the length of the second waveguide is only $2a_2$. Two vertical dashed lines in Fig. 6 are the interfaces between the different PhC segments. In the following, we use the DtN-map method to calculate the resonant mode of the cavity.

As in the previous section, we use two curves Γ_0 and Γ_1 that follow the edges of the hexagon unit cells to terminate the semi-infinite PhC waveguides in the left and right. Assuming the y axis is located at the center of the structure, the two dashed lines are located at $x = \pm a_2$, and Γ_0 and Γ_1 are mirror images of each other. Since the left and right semi-infinite waveguides have regular hexagon unit cells, Γ_0 and Γ_1 consist of edges with length $a_1/\sqrt{3}$. If the frequency is given, we can set up rigorous boundary conditions on Γ_0 and Γ_1. The boundary condition on Γ_1 is still Eq. (9). On Γ_0, the boundary condition should be

$$\frac{\partial u}{\partial \nu} = \mathbf{L}_1^- u, \quad \text{on} \quad \Gamma_0. \tag{12}$$

Comparing with the boundary condition used in the previous section, i.e., Eq. (10), we notice that the above has no inhomogeneous term, since there is no incident wave for the

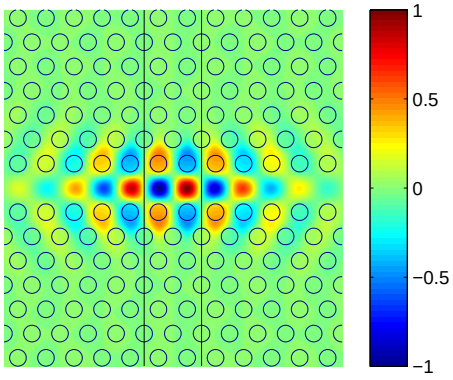

Fig. 7. The magnetic field pattern of a resonant mode of a mode-gap cavity.

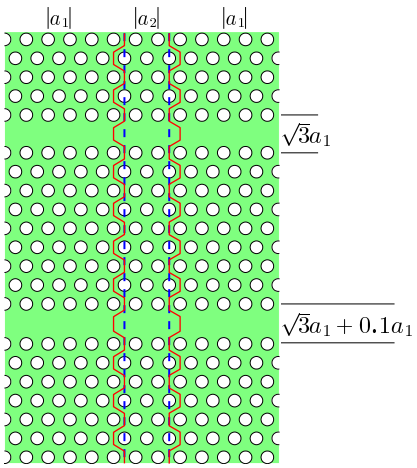

Fig. 8. A mode-gap cavity coupled with the third waveguide shown in Fig. 1(c).

resonant cavity problem. In addition, the operator $\mathbf{L}_1^+$ has a subscript 1 to indicate its link with the first waveguide of Fig. 1.

The region between Γ_0 and Γ_1 can be divided to hexagon unit cells. Those unit cells between the two dashed lines are horizontally stretched hexagons, so that the distance between the two vertical edges is a_2. The special unit cells that cut through the dashed lines are half-regular and half-stretched. The distance between the two vertical edges of a special unit cell is $(a_1+a_2)/2$. For each unit cell in this region, we can find its DtN map. Based on the boundary conditions (9) and (12), the DtN maps of the unit cells, and a zero boundary condition for terminating the y direction, we can set up a homogeneous linear system

$$\mathbf{A}(\omega)\boldsymbol{u} = \mathbf{0}, \tag{13}$$

where $\boldsymbol{u}$ stands for u on the edges of the unit cells between and including Γ_0 and Γ_1. Since the DtN maps of the unit cells and the boundary operators $\mathbf{L}_1^\pm$ all depend on the frequency, the coefficient matrix $\mathbf{A}$ depends on ω. For a resonant mode, the frequency ω is actually to be determined. From Eq. (13), we realize that a non-zero solution $\boldsymbol{u}$ only exists when the matrix $\mathbf{A}$ is singular. This gives us the condition for solving ω. For example, we can solve ω from

$$\lambda_1(\mathbf{A}) = 0, \tag{14}$$

where λ_1 is the eigenvalue of $\mathbf{A}$ with the smallest magnitude. Once ω is solved, a non-zero vector $\boldsymbol{u}$ can be found, and the wave field in any unit cell can be constructed.

Using the same parameters (a_1, a_2, r, n_e, N_t and N_p) as in the previous section, we calculate the resonant frequency of the mode-gap cavity, and obtain $\omega a_1/(2\pi c) = 0.26360047$. The magnetic field of the resonant mode is shown in Fig. 7. Notice that the 2D Helmholtz equation (1) cannot model out-of-slab radiation, thus the cavity confines light without any leakage. Song *et al.* [4] calculated resonant modes of mode-gap cavities fabricated on a silicon slab with a thickness $0.6a_2 = 252\,\text{nm}$, and obtained a Q-factor larger than 2 million for $r = 0.29a_2$.

In order to inject light into the cavity, we need to couple it with a waveguide which has a propagating mode for frequencies around the resonant frequency. As in Ref. [4], we consider the structure shown in Fig. 8, where a PhC waveguide with its core increased by $0.1a_1$ is placed below the mode-gap cavity. Nine rows of air-holes are kept between the cavity and the additional waveguide. Outside the two dashed lines, this additional waveguide is the third waveguide shown in Fig. 1(c), and it supports a propagating mode in the frequency interval F_g. However, with this additional waveguide, the nature of the cavity has changed. Since power can escape from the cavity through the added waveguide, the cavity mode becomes leaky.

The DtN-map method can be used to calculate leaky cavity modes [38]. As shown in Fig. 8, we have two curves Γ_0 and Γ_1 which serve as the boundaries of the semi-infinite PhC waveguides in the left and right sides of the cavity. Notice that the computational domain is significantly extended in the negative y direction to include the new waveguide. The boundary conditions on Γ_0 and Γ_1 can be written down as

$$\frac{\partial u}{\partial \nu} = \mathbf{L}_3^- u \quad \text{on} \quad \Gamma_0, \tag{15}$$

$$\frac{\partial u}{\partial \nu} = \mathbf{L}_3^+ u \quad \text{on} \quad \Gamma_1. \tag{16}$$

We have replaced the operators $\mathbf{L}_1^\pm$ in (12) and (9) by $\mathbf{L}_3^\pm$, since the PhC waveguides in the left and right sides now contain the third waveguide shown in Fig. 1(c). The operators $\mathbf{L}_3^\pm$ depend on the frequency. For a real ω, they can be constructed by the method given in [33], but it is necessary to consider the structure in the left and right as a super-waveguide with two cores. The super-waveguide should have one propagating Bloch mode with a real Bloch wavenumber $\beta_1^{(3)}$ for frequencies in F_g. When the definition of $\mathbf{L}_3^\pm$ is extended to the complex plane, we need to enforce the continuous dependence of the Bloch wavenumbers $\beta_j^{(3)}$ on the imaginary part of ω [38]. For the assumed time dependence $\exp(-i\omega t)$, a leaky cavity mode should have a complex ω with a negative imaginary part, so that as t is increased, the amplitude of the cavity mode decreases exponentially. Meanwhile, for a small negative imaginary part of ω, $\beta_1^{(3)}$ should have a small negative imaginary part, such that the Bloch mode $\phi_1^{(3)} \exp(i\beta_1^{(3)} x)$ blows up as $x \to +\infty$.

As before, the region between Γ_0 and Γ_1 is divided into unit cells, and the linear system (13) with a new $\boldsymbol{u}$ and a new $\mathbf{A}$ can

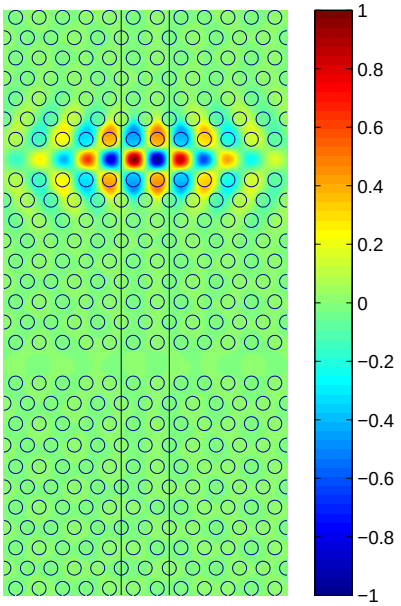

Fig. 9. The magnetic field pattern of a resonant mode of the leaky mode-gap cavity.

be established with the aid of DtN maps of the unit cells and the boundary conditions (15) and (16). However, the matrix $\mathbf{A}$ is non-singular for real ω. Solving Eq. (14), we obtain a complex solution $\omega a_1/(2\pi c) = 0.2636001647 - 0.0000000266i$. The real part gives the resonant frequency, and the imaginary part is related to the quality factor: $Q = 0.5|\mathrm{Re}(\omega)/\mathrm{Im}(\omega)| \approx 5.0 \times 10^6$. Notice that the resonant frequency of the leaky mode is slightly different from that of the non-leaky mode. The magnetic field pattern of the leaky mode is shown in Fig. 9. Although it appears indistinguishable from the one shown in Fig. 7, actually the field blow up in the lower waveguide as $x \to \pm\infty$. For the actual 3D mode-gap cavity on a slab [4], it is expensive to calculate its resonant mode when the additional waveguide is included. Our 2D result could be a relevant indicator for the loss to the waveguide in actual 3D structures.

V. Waveguide-cavity systems

In the previous section, the mode-gap cavity is allowed to couple to a waveguide, but the structure is only studied as a leaky cavity supporting a resonance with a finite Q factor. In this section, we consider the structure as a waveguide-cavity system, and analyze the response of the system when an incident wave is specified in the input waveguide. Mathematically, this leads to a boundary value problem.

As shown in Fig. 8, we have two vertical dashed lines (assuming they are at $x = \pm a_2$) that separate the different PhC segments. The structure for $x < -a_2$ or $x > a_2$ is regarded as a super-waveguide with two cores. Assuming the incident wave is a propagating Bloch mode given in the super-waveguide for $x < -a_2$, we can expand the wave field for

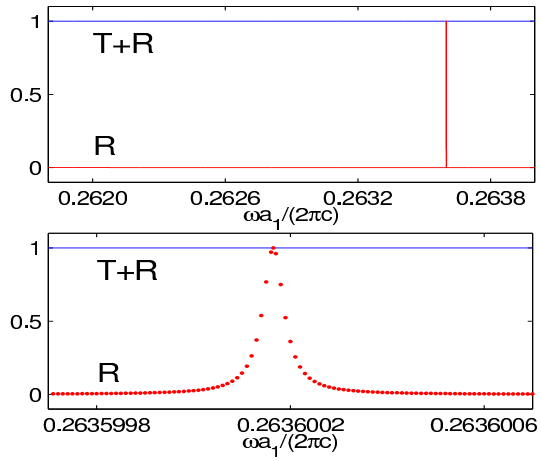

Fig. 10. Reflection spectrum of the waveguide-cavity system shown in Fig. 8.

$|x| > a_2$ as

$$u = \begin{cases} \phi_1^{(3)} e^{i\beta_1^{(3)} x} + \sum_{j=1}^{\infty} B_j \phi_j^{(3)} e^{-i\beta_j^{(3)} x}, & x < -a_2 \\ \sum_{j=1}^{\infty} C_j \phi_j^{(3)} e^{i\beta_j^{(3)} x}, & x > a_2, \end{cases} \tag{17}$$

where $\beta_1^{(3)}$ is real, $\mathrm{Im}(\beta_j^{(3)}) > 0$ for $j \neq 1$, $\phi_j^{(3)}$ is periodic in x with period a_1, B_j and C_j are unknown expansion coefficients. In the above, the reflected and transmitted waves are expanded in the Bloch modes of the super-waveguide. The normalized power reflection and transmission coefficients are simply $|B_1|^2$ and $|C_1|^2$, respectively.

To use the DtN-map method, we need the two curves Γ_0 and Γ_1 shown in Fig. 8 to set up boundary conditions that terminate the semi-infinite waveguides in the left and right. The boundary condition on Γ_0 is essentially the same as (10). We have

$$\frac{\partial u}{\partial \nu} = \mathbf{L}_3^- u + g \quad \text{on} \quad \Gamma_0, \tag{18}$$

where g is related to the incident Bloch mode. The boundary condition on Γ_1 is given in (16). The DtN-map method gives rise to the linear system (11), where $\boldsymbol{u}$ represents u on the edges of the unit cells between Γ_0 and Γ_1, and $\boldsymbol{f}$ is related to the inhomogeneous term in Eq. (18). Based on the same parameters (a_1, a_2, r, n_e, N_t and N_e) as before, we obtain the reflection spectrum shown in Fig. 10. Notice that the reflection coefficient is close to zero except in an extremely narrow frequency range where it has a peak and reaches 1 at $\omega a_1/(2\pi c) = 0.26360016$. The peak frequency is exactly the resonant frequency of the leaky cavity mode shown in Fig. 9.

Song *el al.* [4] fabricated the waveguide-cavity system on a silicon slab of thickness 250 nm, measured the intensity of light as a function of the incident wavelength. A sharp peak similar to the one in Fig. 10 was observed, leading to their estimated experimental Q-factor around $600,000$. A direct numerical simulation for the 3D waveguide-cavity system is difficult. Without a very high resolution, it is impossible to capture the sharp peak in the reflection spectrum related to a resonance with a quality factor above 2 millions.

VI. Conclusion

In this paper, some accurate computational results are presented for a number of PhC heterostructure devices, based on an extended DtN-map method and a 2D Helmholtz equation. The structures considered include PhC waveguides, waveguide discontinuities, mode-gap cavities and a waveguide-cavity system, all in PhC heterostructures. Our study follows the work of Song *et al.* [4] where 3D numerical results for mode-gap cavities (without the input waveguide) and experimental results for the waveguide-cavity system were presented. Although 2D models based on the Helmholtz equation cannot be used to predict out-of-slab radiation losses, our results still have certain similarity with the experimental and 3D numerical results of Song *et al.* [4]. We believe that 2D models are useful for analyzing PhC slab structures, especially when the out-of-slab radiation loss is insignificant.

The DtN-map method was first developed to study basic properties of idealized 2D PhCs [34], [35], but it is particularly efficient for analyzing general PhC devices [33] and leaky cavities [38]. In particular, the method computes a rigorous boundary condition for terminating PhC waveguides, and this has led to very small computational domains. While our previous studies are concentrated on PhC structures with regular hexagon and square unit cells, the examples presented in this paper indicate the the DtN-map method remains highly accurate for slightly deformed unit cells that appear in PhC heterostructures. We believe the method is useful for analyzing more complicated PhC heterostructure devices, and it can be used in the design and optimization process for quickly exploring a large number of design parameters.

References

[1] B. S. Song, S. Noda, and T. Asano, "Photonic devices based on in-plane hetero photonic crystals," Science, vol. 300, pp. 1537, 2003.

[2] B. S. Song, T. Asano, Y. Akahane, Y. Tanaka, and S. Noda, "Transmission and reflection characteristics of in-plane hetero-photonic crystals," Appl. Phys. Lett., vol. 85, no. 20, pp. 4591-4593, 2004.

[3] E. Istrate and E. H. Sargent, "Photonic crystal heterostructures and interfaces," Rev. Mod. Phys., vol. 78, pp. 455-481, 2006.

[4] B. S. Song, S. Noda, T. Asano, and Y. Akahane, "'Ultra-high-Q photonic double-heterostructure nanocavity," Nat. Mater., vol. 4, no. 3, pp. 207-210, 2005.

[5] Y. Taguchi, Y. Takahashi, Y. Sato, T. Asano, and S. Noda, "Statistical studies of photonic heterostructure nanocavities with an average Q factor of three million," Opt. Express, vol. 19, no. 12, pp. 11916-11921, 2011.

[6] H. Sekoguchi, Y. Takahashi, T. Asano, and S. Noda, "Photonic crystal nanocavity with a Q-factor of $\sim$9 million," Opt. Express, vol. 22, no. 1, pp. 916-924, 2014.

[7] B. S. Song, T. Asano, Y. Akahane, Y. Tanaka, and S. Noda, "Multi-channel add/drop filter based on in-plane hetero photonic crystals," J. Lightw. Technol., vol. 23, pp. 1449-1455, 2005.

[8] H. Takano, B. S. Song, T. Asano, and S. Noda, "Highly efficient multi-channel drop filter in a two-dimensional hetero photonic crystal," Opt. Express, vol. 14, no. 8, pp. 3491-3496, 2006.

[9] Y. Takahashi, T. Asano, D. Yamashita, and S. Noda, "Ultra-compact 32-channel drop filter with 100 GHz spacing," Opt. Express, vol. 22, no. 4, pp. 4692-4698, 2014.

[10] P. Lalanne, C. Sauvan, and J. P. Hugonin, "Photon confinement in photonic crystal nanocavities," Laser & Photon. Rev., vol. 2, no. 6, pp. 514-526, 2008.

[11] M. Nomura, K. Tanabe, S. Iwamoto, and Y. Arakawa, "High-Q design of semiconductor-based ultrasmall photonic crystal nanocavity," Opt. Express, vol. 18, pp. 8144-8150, 2010.

[12] X. Liang and S. G. Johnson, "Formulation for scalable optimization of microcavities via the frequency-averaged local density of states," Opt. Express, vol. 21, pp. 30812-30841, 2013.

[13] J. Berenger, "A perfectly matched layer for the absorption of electromagnetic waves," J. Comput. Phys., vol. 114, pp. 185-200, 1994.

[14] W. C. Chew and W. H. Weedon, "A 3-D perfectly matched medium from modified maxwell's equations with stretching coordinates," Micro. Opt. Tech. Lett., vol. 7, pp. 599-604, 1994.

[15] A. F. Oskooi, L. Zhang, Y. Avniel, and S. G. Johnson, "The failure of perfectly matched layers, and towards their redemption by adiabatic absorbers," Opt. Express, vol. 16, pp. 1137611392, July 2008.

[16] A. Oskooi and S. G. Johnson, "Distinguishing correct from incorrect PML proposals and a corrected unsplit PML for anisotropic, dispersive media," J. Comput. Phys., vol. 230, pp. 23692377, April 2011.

[17] H. Benisty, D. Labilloy, C. Weisbuch, C. J. M. Smith, T. F. Krauss, D. Cassagne, A. Beraud, and C. Jouanin, "Radiation losses of waveguide-based two-dimentional photonic crystals: Positive role of substrate," Appl. Phys. Lett., vol. 76, no. 5, pp. 532-534, 2000.

[18] M. Qiu, "Effective index method for heterostructure-slab-waveguide-based two-dimensional photonic crystals," Appl. Phys. Lett., vol. 81, no. 7, pp. 1163-1165, 2002.

[19] L. Yang, J. Motohisa, and T. Fukui, "Suggested procedure for the use of the effective-index method for high-index-contrast photonic crystal slabs," Optical Engineering, vol. 44, no. 7, 078002, 2005.

[20] M. Dems and W. Nakwaski, "The modelling of the high-contrast photonic crystal slabs using the novel extension of the effective index method," Optica Applicata, vol. 36, no. 1, pp. 51-56, 2006.

[21] W. Zhou, Z. Qiang, and L. Chen, "Photonic crystal defect mode cavity modelling: a phenomennological dimeional reduction approach," Journal of Physics D: Applied Physics, vol. 40, pp. 2615-2633, 2007.

[22] M. Hammer and O. V. Ivanova, "Effective index approximations of photonic crystal slabs: a 2-to-1-D assessment," Opt. Quant. Electron., vol. 41, no. 4, pp. 267-283, 2009.

[23] O. V. Ivanova, R. Stoffer, and M. Manfred, "A dimensionality reduction technique for 2D scattering problems in photonics," Journal of Optics, vol. 12, no. 3, 035502, 2010.

[24] P. Bindal and A. Sharma, "Modelling of photonic crystal waveguides: a simple and accurate approach," Opt. Quant. Electron., vol. 42, no. 8, pp. 435-446, 2011.

[25] S. Zhang, W. Zhou, X. Ye, Bo. Xu, and Z. Wang, "Cavity-mode calculation of L3 photonic crystal slab using the effective index perturbation method," Optical Review, vol. 20, no. 5, pp. 420-425, 2013.

[26] A. Taflove and S. C. Hagness, *Computational Electrodynamics: The Finite-Difference Time-Domain Method*, 3rd ed. Artech House, 2005.

[27] J. S. Hesthaven and T. Warburton, "Nodal high-order methods on unstructured grids: I. time-domain solution of Maxwell's equations," J. Comput. Phys., vol. 181, pp. 186-221, 2002.

[28] T. Lu, P. Zhang, and W. Cai, "Discontinuous Galerkin methods for dispersive and lossy Maxwell's equations," J. Comput. Phys., vol. 200, no. 2, pp. 549-580, 2004.

[29] J. Niegemann, M. König, and K. Busch, "Discontinuous Galerkin methods in nanophotonics," Laser & Photonics Reviews, vol. 5, no. 6, pp. 773-809, 2011.

[30] J. Jin, *The Finite Element Method in Electromagnetics*, 2nd ed., Wiley, 2002.

[31] D. Felbacq, G. Tayeb, and D. Maystre, "Scattering by a random set of parallel cylinders," J. Opt. Soc. Am. A, vol. 11, pp. 2526-2538, 1994.

[32] J. Smajic, C. Hafner, and D. Erni, "Design and optimization of an achromatic photonic crystal bend," Opt. Express, vol. 11, pp. 1378-1384, 2003.

[33] Z. Hu and Y. Y. Lu, "Efficient analysis of photonic crystal devices by Dirichlet-to-Neumann maps," Opt. Express, vol. 16, pp. 17383-17399, 2008.

[34] Y. Huang and Y. Y. Lu, "Scattering from periodic arrays of cylinders by Dirichlet-to-Neumann maps," J. Lightw. Technol., vol. 24, pp. 3448-3453, 2006.

[35] J. Yuan and Y. Y. Lu, "Photonic bandgap calculations using Dirichlet-to-Neumann maps," J. Opt. Soc. Am. A, vol. 23, pp. 3217-3222, 2006.

[36] Y. Huang, Y. Y. Lu, and S. Li, "Analyzing photonic crystal waveguides by Dirichlet-to-Neumann maps," J. Opt. Soc. Am. B, vol. 24, pp. 2860-2867, 2007.

[37] S. Li and Y. Y. Lu, "Computing photonic crystal defect modes by Dirichlet-to-Neumann maps," Opt. Express, vol. 15, pp. 14454-14466, 2007.

[38] S. Li and Y. Y. Lu, "Efficient method for analyzing leaky cavities in two-dimensional photonic crystals," J. Opt. Soc. Am. B, vol. 26, pp. 2427-2433, 2009.